Advanced Materials Interfaces

ADVANCED MATERIALS INTERFACES Open Access

www.advmatinterfaces.de

RESEARCH ARTICLE OPEN ACCESS

Assessing the Mechanism of NH_3 Sensing in Flexible Carbon-Nanotube-Based Chemoresistive Sensors via In Situ Photoemission Spectroscopy

Christos Gatsios[1] | Antonello Mascia[2] | Cristian Tomasi Cebotari[1,3] | Sahira Vasquez[4] | Zygmunt Milosz[5] | Andrea Pedrielli[6] | Matteo Amati[5] | Luca Gregoratti[5] | Luisa Petti[4] | Piero Cosseddu[2] | Luca Pasquali[7,8,9] | Melanie Timpel[1] | Marco V. Nardi[1]

[1]IMEM-CNR, Institute of Materials for Electronics and Magnetism, Trento, Italy | [2]Department of Electrical and Electronics Engineering, University of Cagliari, Cagliari, Italy | [3]Department of Chemistry, Life Science and Environmental Sustainability, University of Parma, Parma, Italy | [4]Sensing Technologies Laboratory (STL), Faculty of Engineering, Free University of Bozen-Bolzano, Bolzano, Italy | [5]Elettra Sincrotrone Trieste S.C.p.A., Trieste, Italy | [6]Sensors and Devices Center, Fondazione Bruno Kessler, Trento, Italy | [7]Department of Engineering "Enzo Ferrari", University of Modena and Reggio Emilia, Modena, Italy | [8]CNR-Istituto Officina dei Materiali (IOM), Trieste, Italy | [9]Department of Physics, University of Johannesburg, Johannesburg, South Africa

Correspondence: Christos Gatsios (christosgatsios@cnr.it) | Melanie Timpel (melaniekristina.timpel@cnr.it) | Marco V. Nardi (marcovittorio.nardi@cnr.it)

Received: 25 September 2025 | **Revised:** 18 November 2025 | **Accepted:** 3 December 2025

Keywords: carbon nanotubes | electronic properties of surfaces | flexible chemical sensors | surface spectroscopies | transduction mechanisms

ABSTRACT

Flexible carbon nanotube (CNT) chemoresistors offer a scalable, low-cost platform for wearable gas detection. However, a clear understanding of their sensing mechanism remains essential to optimize sensitivity, selectivity, and overall reliability. In this work, we complement electrical response measurements in both dry air and ultra-high vacuum (UHV) with synchrotron-based in situ X-ray photoelectron spectroscopy (XPS) to directly probe ammonia (NH_3)–CNT interactions. In both environments, the response can be described by Langmuir-type adsorption–desorption kinetics. In dry air (3–50 ppm), the devices exhibit a reproducible increase in resistance with a sensitivity of ~0.4% ppm^{-1}. Under UHV, a nominal NH_3 concentration of ~8 ppm produces a smaller relative response of ~0.5%, comparable to that obtained at 3 ppm in dry air. In situ micro-focused XPS reveals reversible (≈1 eV) shifts in the C 1s core-level binding energy during NH_3 exposure, confirming that NH_3 acts as an electron donor. This spectroscopic evidence correlates quantitatively with the chemoresistive response, establishing intra-CNT charge transfer as the dominant transduction mechanism. These findings underscore the effectiveness of coupling XPS with electrical analysis to unravel gas-sensor transduction in nanomaterials and pave the way for the rational design of high-performance CNT-based sensors.

1 | Introduction

Carbon nanotubes (CNTs) have emerged as highly promising materials for scalable gas sensing applications due to their exceptional sensitivity and rapid response times, which remain effective even at room temperature [1, 2], unlike conventional metal-oxide based sensors that typically require elevated operating temperatures [3]. In parallel, CNT-based chemoresistors as well as alternative gas-sensing platforms based on metal-oxide systems and 2D semiconductors have been explored for detecting environmentally and industrially relevant gases such as NO_2, CO, H_2, and various volatile organic compounds, underscoring the growing need for reliable gas-monitoring technologies [4–6]. Within this broader landscape, CNT-based chemoresistive sensors offer tunable conductivity and mechanical flexibility while enabling simple, low-cost fabrication and miniaturization

potential [7–9]. Despite their poor selectivity, recent works have also demonstrated that careful covalent or non-covalent functionalization strategies, such as polymer coatings or metal nanoparticle decorations, can impart selectivity capabilities to CNTs for various analytes [10, 11].

The chemoresistive sensing mechanism of CNT-based sensors has usually been attributed to: i) intra-CNT interactions, namely charge transfer between the analyte and individual CNTs, ii) inter-CNT interactions such as changes in the spacing between adjacent CNT sidewalls, and iii) Schottky barrier modulations at the CNT-electrode interface [8, 12]. However, distinguishing which of these possibilities dictates device response remains a subject of interest, and it depends on both material and device characteristics. For example, it has been shown that inter-CNT interactions become considerable in devices comprising of a network of CNTs [13, 14], while the electronic character of CNTs, defined by the position of the Fermi level relative to the electronic density of states, can be substantially influenced by the content of defects, impurities or functionalization strategies, leading to varied device responses [15–18]. Electrical measurements have been the primary tool to observe sensing behavior, but even though two-terminal devices readily capture resistance changes, they do not explicitly reveal which of the mechanisms dominates under a given condition [2, 19].

In recent years, device miniaturization has driven the need for advanced spectroscopic techniques to reveal electronic behavior at micro- and nanoscale dimensions. For example, scanning photoelectron spectroscopy has directly tracked charge transfer between NO_x and MoS_2 in gas-sensor field-effect transistors [20]. By contrast, studies of CNTs have largely relied on ex situ Raman spectroscopy and X-ray photoelectron spectroscopy (XPS) to assess chemisorbed species after gas exposure [21–23]. In situ spectroscopic investigations of CNTs based chemorestive devices, complemented by electrical measurements to capture adsorption–desorption dynamics during gas exposure, are still lacking [24, 25].

Micro-focused XPS under controlled gas atmosphere is a powerful technique for directly observing the electronic core-levels during gas exposure [26, 27]. By monitoring binding energy shifts of the core levels, one can capture surface charge transfer processes associated with intra-CNT interactions between the CNTs and the analyte gas. Notably, core-level shifts are predominantly influenced by local electronic environments and are less affected by inter-CNT interactions, such as changes in inter-tube distances. Furthermore, by focusing the X-ray beam on the device's sensing region, spatially resolved investigations become possible, enabling correlation of the device response with resistance modulation within the sensing material, as opposed to Schottky barrier modulations occurring at the electrode interfaces.

Sensing NH_3 in concentrations lower than 25 ppm presents valuable early-warning detection, since occupational safety regulations typically set exposure limits in the 25–50 ppm range, with 25 ppm already considered hazardous over time. A previous theoretical study predicted that NH_3 adsorption on single-walled CNTs induces electron transfer from NH_3 to the CNTs [28]. In CNTs exhibiting p-type conductivity, electron donation is expected to cause an increase in electrical resistance. Indeed, several experimental works using semiconductive single-walled CNTs spray-coated on flexible polyimide (PI) substrates have reported an increase in resistance upon each NH_3 exposure [29–32]. In contrast, common interfering gases or ions induce significantly lower charge transfer with the CNT networks, thus smaller responses [33, 34].

Although studies on CNT-based gas sensors have been widely reported, most of them focus primarily on improving device architecture or optimizing performance metrics, while the fundamental surface processes occurring during gas exposure remain insufficiently addressed [7, 8]. In this work, we investigate these intrinsic mechanisms by correlating the resistive response of flexible CNT-based chemoresistors with in situ XPS during controlled NH_3 dosing. Using the dynamic high-pressure NH_3 system available at the ESCAmicroscopy beamline of the Elettra synchrotron [35], we observe significant binding energy shifts of up to 1 eV in the C 1s core level during NH_3 adsorption. We attribute these shifts primarily to charge-transfer processes associated with reversible Langmuir-type adsorption–desorption kinetics of NH_3 molecules on the CNT surface, with a smaller contribution from irreversible chemisorption. In other words, the electron-donating NH_3 molecules effectively decrease the hole concentration, leading to a downward shift in all electronic core levels consistent with previous findings [36, 37].

While our XPS measurements are performed under ultra-high vacuum (UHV) conditions, which are necessary for the technique, they remain directly relevant to gas sensors operating in ambient conditions. As shown in our comparative measurements, adsorption–desorption kinetics in dry air can indeed become slower due to competing gas interactions, yet the underlying charge transfer mechanism, namely the formation of a surface depletion layer and the resulting increase in resistance, remains consistent. Our spatially resolved measurements thus support intra-CNT charge modulation as the primary transduction mechanism for NH_3 sensing in these CNT devices. Moreover, the use of fully scalable fabrication, namely spray-coating CNT networks onto flexible PI substrates and screen-printing silver electrodes, demonstrates that technologically relevant devices can serve as simple yet innovative model systems for fundamental studies, paving the way toward more reliable gas-sensing technologies. To our knowledge, this is the first systematic study that complements electrical response measurements with in situ XPS signatures of surface charge transfer interactions between NH_3 and CNT networks.

2 | Results and Discussion

2.1 | Chemoresistive Response of CNT Films During NH_3 Exposure in Dry Air

Figure 1a–c shows the device architecture of our CNT-based chemoresistors. Scanning electron microscopy (SEM) images (Figure S1a,b) reveal a randomly oriented, interconnected network of CNTs forming the sensing film, consistent with atomic force microscopy images reported in previous works [30]. Individual CNT bundles appear uniformly distributed across the

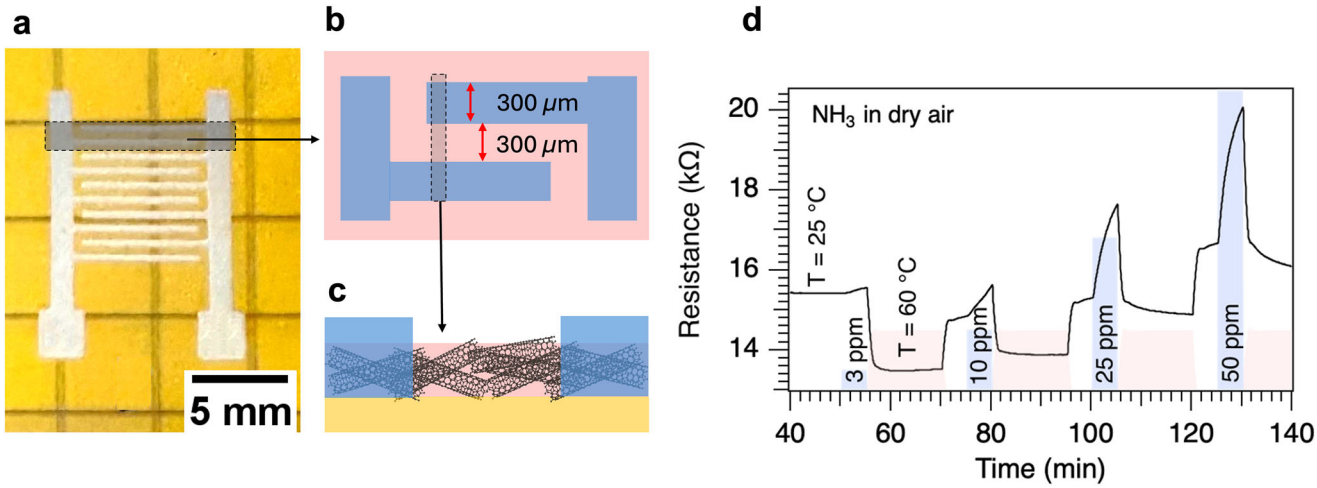

FIGURE 1 | a) Photograph of the flexible CNT-based NH_3 sensor. b) Schematic illustration of the interdigitated silver electrodes (300 μm finger width), screen-printed over the CNTs to form the resistive sensor. c) Cross-sectional illustration showing the CNT network agglomerated within the interdigitated spacing region, forming a porous film that bridges the interdigitated Ag electrodes. d) Dynamic resistance response of CNT-based sensors upon exposure to increasing NH_3 concentrations (3–50 ppm) in dry air. Blue shaded regions indicate NH_3 dosing at the specified concentration, while red shaded regions mark active recovery steps at 60 °C for 15 min.

polyimide substrate with minimal agglomeration, confirming that the water-based dispersion and deposition process effectively prevented CNT clustering. This percolative structure provides multiple conductive pathways, ensuring stable baseline conductivity and enabling robust signal modulation during gas exposure. Figure 1d shows the dynamic resistance response upon exposure to increasing NH_3 concentrations (3–50 ppm) in dry air at room temperature. After each NH_3 exposure, the sensor undergoes an active recovery at 60 °C for 15 min, followed by cooling back to 25 °C before the next gas pulse [29, 30]. Following this heating step, as the sensor cools down to room temperature (25 °C), prior to gas exposure, the resistance gradually increases due to the reduction in thermal carrier mobility, an effect clearly visible as a pre-exposure upward trend in the resistance curve. Upon NH_3 injection, a further resistance increase is observed, with the response magnitude correlating to gas concentration. Despite this thermal treatment, a gradual upward drift of the baseline resistance is observed over successive cycles. This trend may be indicative of partial chemisorption or irreversible surface interactions, leading to cumulative changes in CNT surface chemistry.

As the NH_3 concentration increases, the normalized response ($\Delta R/R_i$, where R_i is the baseline resistance immediately before dosing and ΔR is the total resistance change from start to end of dosing) grows monotonically, reaching ~20 % at 50 ppm. Notably, the 25 and 50 ppm curves display well-defined adsorption plateaus, whereas the 10-ppm curve exhibits a more gradual, quasi-linear response without clear saturation within the measurement window. These observations reflect the expected scaling of adsorption kinetics with analyte concentration: higher NH_3 doses accelerate site occupancy and reveal the characteristic exponential response shape, while at low concentrations the kinetics become slower and more difficult to distinguish from noise. This trend is consistent with the impedance spectra shown in Figure S2, where the low-frequency magnitude remains purely resistive and shifts upward with increasing NH_3 concentration.

To assess the stability and reusability of the CNT-based sensors, they were subjected to four consecutive measurement cycles at 3 ppm NH_3 under identical conditions (see Figure S3a), demonstrating consistent repeatability and minimal variation across repeated exposures. A rough estimate of the sensor's detection limit (see Figure S3b,c) is approximately 1 ppm.

In agreement with previous reports on spray-coated CNT films on flexible substrates [29, 30], these CNT-based sensors exhibit the expected concentration-dependent and reversible resistive response to NH_3, with reproducible performance over multiple cycles. The observed response shapes, saturation trends, and repeatability collectively indicate that our CNT network provides a stable and reliable platform for quantitative gas sensing.

2.2 | Adsorption–Desorption Kinetics: Comparison of UHV and Dry Air Environments

To directly compare the response of our CNT sensors in different environments, we also investigated their behavior under UHV conditions using controlled NH_3 dosing. Figure 2a shows the dynamic resistance response of the CNT-based chemoresistors to 8 ppm NH_3 in UHV. The baseline resistance in UHV is ~25 kΩ, significantly higher than the ~15 kΩ baseline observed in dry air (Figure 1d). This shift can be attributed to the absence of O_2 under vacuum conditions, as oxygen is known to act as an electron acceptor, enhancing the p-type conductivity of CNTs by increasing hole concentration [36]. Without O_2, the effective hole concentration is reduced, leading to a higher baseline resistance.

Upon exposure to a nominal NH_3 concentration of 8 ppm in UHV (as determined in Note S1), the device exhibits a relative response of ~0.5 %, comparable to the response obtained at 3 ppm in dry air. This likely suggests that oxygen in ambient conditions enhances NH_3 adsorption by maintaining a higher initial hole concentration at the CNT surface. Interestingly, the inset of

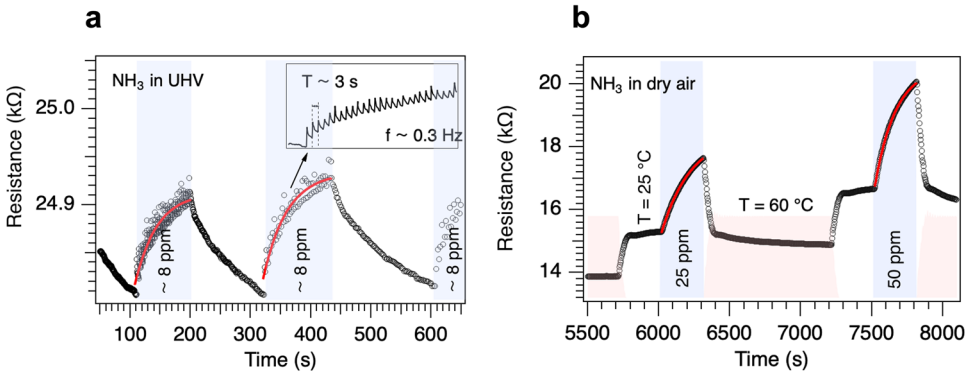

FIGURE 2 | a) Resistive response of CNT-based sensors in UHV upon repeated exposure to a nominal NH_3 concentration of ~8 ppm (0.3 Hz valve repetition, 2.42 ms aperture). The response shows large resistance modulations associated with progressive surface saturation, while rapid oscillations at 0.3 Hz match the valve frequency, indicating a fast dynamic sensor response on a timescale of $\tau < 1.5$ s. b) Comparison with dry-air measurements. Red lines correspond to Langmuir-model fits of the adsorption response curves in UHV and dry air.

Figure 2a reveals small periodic modulations of the resistance at a frequency of 0.3 Hz, identical to the repetition rate of the dosing valve. This indicates that the CNT network responds within each valve cycle, corresponding to an intrinsic response time shorter than ~1.5 s. Such rapid modulation supports the notion of very fast charge-transfer interactions.

To analyze the kinetics more quantitatively, we applied the Langmuir adsorption model introduced previously [38–40], with the full derivation provided in Note S2. Within this framework, the reactions of NH_3 on the CNT surface can be expressed by reversible adsorption-desorption processes,

$$NH_{3(g)} + S_v \rightleftharpoons S_a \tag{1}$$

where S_v denotes a vacant site and S_a an adsorbed site. Assuming the resistance is a linear function of surface coverage, the resistance during adsorption evolves according to,

$$R_a(t) = R_i + \Delta R_\infty \left[1 - \exp\left(-\frac{t - t_0}{\tau_a}\right)\right] \tag{2}$$

where R_i is the baseline resistance before NH_3 dosing, ΔR_∞ is the maximum resistance change at saturation, t_0 is the time at which NH_3 dosing starts, and τ_a is the adsorption time constant. This model was used to fit our experimental response curves.

The response curves at 25 and 50 ppm in dry air correspond to well-defined adsorption plateaus and enabled reliable fitting of the Langmuir model, as shown in Figure 2b, yielding τ_a with reasonably small errors. Despite the small relative response in UHV at 8 ppm, the curves reached sufficient saturation to allow reliable fitting, as illustrated in Figure 2a, yielding an adsorption time constant of 37 ± 2 s. In comparison, dry-air measurements gave an average adsorption time constant of 251 ± 1 s. This order-of-magnitude difference highlights the effect of the surrounding gases in dry air that slow down adsorption, whereas the absence of competing species under vacuum conditions facilitates faster adsorption–desorption kinetics.

Note that the recovery kinetics of the sensor cannot be directly compared across the different environments in our experiments. In dry air, recovery was actively assisted by heating the sensor to 60 °C, whereas in UHV no heating was applied following each dosing cycle. Thus, recovery in dry air reflects thermally enhanced desorption in the presence of oxygen, while recovery in UHV corresponds to passive desorption in an oxygen-free environment. For this reason, only the adsorption kinetics are compared quantitatively. Overall, the sensors exhibit qualitatively similar behavior in both environments, allowing a consistent description within the Langmuir adsorption framework. This also indicates that the in situ XPS analysis under UHV conditions provides mechanistic insights that remain relevant for devices operating under ambient conditions.

2.3 | Charge-Transfer–Induced Modulation of CNT Network Conductivity

To elucidate the surface chemical phenomena underlying the resistive behavior of our CNT sensors, we performed in situ XPS experiments using a micro-focused beam. Figure 3a shows the photoelectron intensity map obtained at 286.3 eV, corresponding to the binding energy region of the C 1s core level. As expected, two distinct regions are evident: i) the CNT sensing region within the interdigitated spacing, covering the PI substrate (red), and ii) the screen-printed Ag electrodes (blue), where minimal or no carbon signal is expected.

High-resolution XPS spectra of the C 1s core level were recorded with the synchrotron beam spot focused on a region where the C 1s signal was more uniform, as indicated by the solid circle in Figure 3b. Figure 3b also shows areas of lower intensity (whiter regions) within the CNT films between the interdigitated electrodes, which can be attributed to topographical contrasts likely due to incomplete coverage of the PI substrate, consistent with SEM images in Figure S1a,b also revealing uncovered regions of the PI substrate.

Figure 3c shows the XPS spectra before, during, and after NH_3 dosing. Before NH_3 dosing, i.e., in the pristine CNTs, the C 1s peak is deconvoluted into three Voigt components, using an active Shirley background to account for secondary-electron contributions to the photoelectron intensity. In this way, without gas,

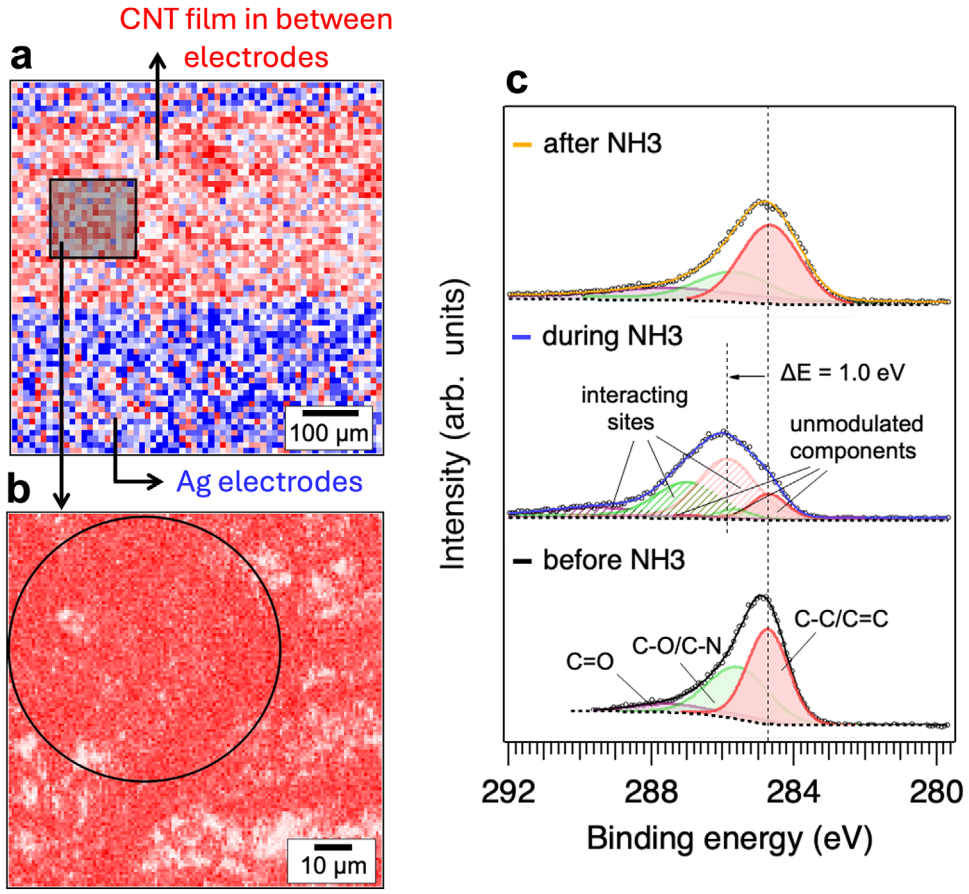

FIGURE 3 | a) SPEM map of the device interdigitated spacing region, collected at the energy region of the C 1s core level (286.3 eV). The CNT-covered sensing region appears in red, corresponding to a high C 1s signal, whereas the interdigitated Ag electrodes, shown in blue, have minimal C 1s intensity. b) Higher-magnification SPEM map of the shaded region in panel a). The solid circular line indicates the 75 µm beam spot used for XPS spectral acquisition. c) High-resolution C 1s XPS spectra recorded before, during, and after dosing with ~8 ppm NH_3 in UHV. The pristine spectrum (black) is deconvoluted into three components: sp2 C—C/C=C (~284.4 eV), C—O/C—N (~286 eV), and C=O (~288 eV). Upon NH_3 exposure (blue), the spectrum is deconvoluted by three static components reflecting the unmodulated components (solid areas) and three dynamic components shifted by ≈1 eV to higher binding energy, indicating the interacting sites (dashed areas). After dosing (yellow), the spectrum returns to its original position, and the dynamic components essentially vanish.

the C 1s spectrum is dominated by three components: the main sp^2 C—C/C=C component at ≈284.4 eV, with additional peaks at ≈286 and ≈288 eV arising from C—O/C—N and C=O species, respectively. These higher-energy components are consistent with the O 1 and N 1s signals observed in the XPS spectra and survey scans prior to NH_3 exposure (Figures S1, S4 and S5) and are most likely associated with photoelectron contributions from uncovered PI substrate regions, surface contaminants introduced during ambient handling, and residual carboxylic acid groups in the CNTs (1–3 at.%, consistent with the supplier's CNT purity of ≥90%).

During NH_3 dosing, the C 1s peak broadens significantly and its maximum shifts by ≈1 eV toward higher binding energy. The spectrum was recorded in the saturation regime, where the resistance no longer changes and the N 1s peak remains constant over consecutive scans, as shown in Figure S4. Under these steady-state conditions in which adsorption and desorption processes equilibrate, it is possible to reliably deconvolute the spectrum using Voigt profiles. In contrast, fitting the spectrum during dosing requires three additional dynamic components associated with interacting sites, in addition to the three static unmodulated components already present in the pristine CNTs. These dynamic contributions, indicated by the dashed areas in Figure 3c, vanish once dosing ceases, with the main peak returning to 284.4 eV. Notably, during dosing, the dynamic components of the interacting sites shift uniformly by ≈1 eV to higher binding energies, while a small fraction of the corresponding static components remains at their initial binding energy. This residual, unshifted signal may result from the fact that not all CNT surfaces interact equally with NH_3. The unmodulated components most likely originate from photoelectrons emitted from uncovered regions of the PI substrate (see Figure S1a), which do not respond to NH_3. In addition, uneven gas coverage, the presence of chemically inert or passivated regions caused by surface contamination, or contributions from deeper CNT layers that are less affected by surface interactions could further account for the static peaks.

After NH_3 dosing, the C 1s maximum returns to its pristine position; however, the overall peak remains slightly broader than before NH_3 exposure. The peak broadening can be associated with

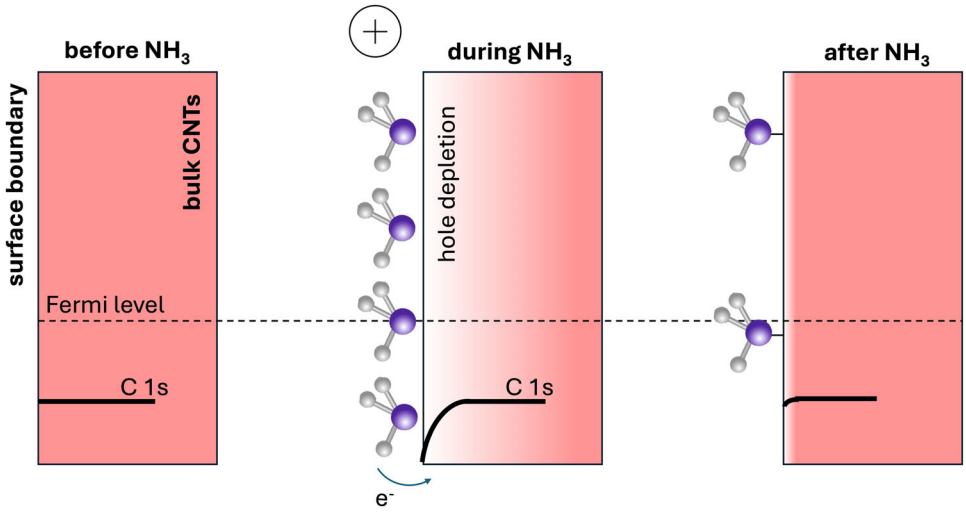

FIGURE 4 | Illustration of the charge transfer mechanism underlying the chemoresistive response in CNT-based sensors. a) Before NH_3 dosing, the C 1s binding energy is uniform across the CNT film, indicating a flat-band condition and a homogeneous hole distribution. b) During NH_3 exposure, adsorbed NH_3 molecules donate electrons to the CNT surface, creating a near-surface hole-depletion region. This induces a downward band bending, shifting the C 1s level by 1 eV away from the Fermi level, while deeper CNT layers remain unaffected. c) After dosing, NH_3 desorption restores the initial hole distribution and flat-band condition, returning the C 1s peak to its original position. The small residual broadening observed in XPS may reflect the presence of chemisorbed NH_3.

the residual N 1s signal that remains detectable after NH_3 dosing (Figure S4), suggesting stronger NH_3 adsorption or chemisorption processes, potentially occurring at defect sites, which are also likely responsible for the gradual baseline resistance increase observed in Figure 1d.

Our observations, specifically, the significant 1 eV shift of the C 1s core level and the corresponding changes in resistance, are consistently explained by reversible surface charge-transfer processes induced by NH_3 adsorption on the CNTs, as schematically illustrated in Figure 4. Before exposure, the C 1s binding energy is uniform across the CNT film, reflecting a homogeneous distribution of hole carriers on the surface. Upon NH_3 dosing, NH_3 molecules adsorb onto the CNT surface and donate electrons to the CNTs. Since CNT conduction is dominated by holes, donated electrons decrease the near-surface hole density. In the case of the C 1s peak, this appears as a change in the shape of the peak and the emergence of dynamic components that vanish once NH_3 dosing stops. The small fraction of the original C—C signal that remains unshifted may indicate heterogeneous surface interactions due to factors such as partial NH_3 coverage, chemically inactive or passivated regions, and unresponsive deeper CNT layers. After dosing, NH_3 desorbs, holes re-populate the surface, and the C 1s peak returns to its original binding energy, providing evidence of predominantly fast NH_3 adsorption and reversible charge-transfer processes. The slight residual broadening observed in the post-exposure spectrum suggests that a small amount of NH_3 may chemisorb at defect or functional-group sites, which can be associated with the gradual baseline resistance drift observed in electrical measurements.

Within this electron-transfer framework, the sensor's resistive response can be related to the shift ΔE of the C 1s core-level using simplistic models from semiconductor physics [41]. Accordingly, the resistive response ($\Delta R/R_i$) can be expressed in terms of the binding energy shift (ΔE) as,

$$\frac{\Delta R}{R_i} \sim \frac{p_i}{p_f} - 1 \sim \exp\left[\frac{\Delta E}{k_B T}\right] - 1 \tag{3}$$

The derivation of Equation 3 is provided in Note S3. Hence, in the first approximation, the resistive response is directly proportional to the material's binding energy shift observed in XPS. Even though this corresponds to a rough estimation, it captures the qualitative trend, suggesting a significant increase in resistance, which should correspond to a significant sensor response for the $\Delta E = 1$ eV shift observed in our XPS measurement. However, we observe only a 0.5% change for 8 ppm of NH_3 on CNTs.

The relatively small change in resistance and small response, despite the pronounced C 1s binding-energy shifts, can be understood by considering two effects that can contribute to this result. First, NH_3 adsorption depletes holes only within a thin surface region of the CNTs, causing that region's resistance to significantly increase, yet the intrinsically low resistance of the deeper CNT layers remains largely unaffected and continues to carry most of the current. In other words, even a highly resistive surface region can be effectively bypassed by bulk conduction channels within the deeper layers of the CNT network. Second, our XPS deconvolution, specifically the ratio of the shifted dynamic C 1s component to the total C 1s area, suggests that about 71% of the probed surface area (Figure 3b) actively interacts with NH_3. As previously mentioned, the remaining unmodulated components may be attributed not only to photoelectron contributions from uncovered regions of the PI substrate but also to CNT areas that do not interact equally with NH_3. These could include chemically inert or passivated regions caused by surface contamination, uneven gas coverage, or deeper CNT layers less affected by surface interactions. Therefore, chemically inert or passivated regions (from surface contamination) and incomplete NH_3 coverage could further limit the number of occupied adsorption sites, reducing the net electron transfer to the CNTs. Moreover, under ambient conditions, the presence of oxygen in dry air could

enhance surface activity by depleting electrons from the CNTs and thereby promoting charge transfer with electron-donating NH_3, as observed in metal oxides [42–44]. However, under the vacuum conditions of our experiment, this effect is absent and may also contribute to the smaller-than-expected response.

Taken together, the combined electrical and in situ XPS results demonstrate that the NH_3 sensing mechanism in CNT networks is governed by reversible charge-transfer interactions and the formation of a surface depletion layer that controls network conductivity, rather than by permanent chemical modification. These processes are enabled by fast adsorption–desorption kinetics, which give rise to measurable and fully reversible C 1s binding-energy shifts and corresponding resistance changes, consistent with the observed recovery of the sensor at room temperature (UHV) or upon mild heating (dry air).

3 | Conclusion

In this study, we have demonstrated a comprehensive investigation of NH_3 sensing by flexible technologically relevant CNT-based chemo-resistive sensors through in situ micro-focused XPS under controlled gas exposure conditions and corresponding electrical characterization under both dry air and UHV conditions. Comparison of dry-air and UHV environments shows that adsorption follows Langmuir-type kinetics in both cases, but proceeds an order of magnitude faster under UHV, where the absence of competing gases facilitates charge transfer. Our combined results reveal a direct correlation between the sensor's chemoresistive response and significant, reversible shifts in the C 1s core-level binding energy, suggesting that intra-CNT charge-transfer processes contribute significantly to the sensing mechanism. The electron donation from NH_3 molecules leads to a transient depletion of hole carriers near the CNT surface, inducing downward band bending and a corresponding increase in electrical resistance consistent with p-type semiconductor behavior. Our findings of the very fast and reversible nature of these charge-transfer interactions underpin the very fast sensor response and recovery times observed. Moreover, residual spectral broadening after NH_3 exposure suggests a minor contribution from chemisorption at defect sites, which aligns with gradual baseline resistance drift seen in repeated sensing cycles. Overall, this work advances the fundamental understanding of charge-transfer dynamics in CNT-based gas sensors and supports the continued development of scalable, low-power, and highly sensitive chemo-resistive devices based on technologically relevant materials for real-time gas detection applications.

4 | Experimental Section

4.1 | Device Fabrication

As described in a previous study [30], the fabrication of flexible CNT-based chemoresistors (Figure 1a) was carried out through a multi-step process optimized for surface uniformity and electrical performance. Initially, PI foil substrates were subjected to a sequential cleaning protocol involving immersion in acetone followed by isopropanol, each step lasting 5 min under sonication to remove organic residues. The cleaned substrates were then dried at 200 °C for 24 h to eliminate solvent traces. To enhance the surface energy and promote better adhesion of the sensing film, the dried PI substrates were exposed to oxygen plasma (Diener electronics, GmbH & Co. KG) treatment under controlled conditions (0.4 mbar pressure, 100 W power, 1-min exposure). This step introduced polar functional groups on the surface, facilitating uniform deposition of the active material [45]. Aqueous dispersions of CNTs (0.05 wt%) stabilized with carboxymethyl cellulose (CMC) were prepared via ultrasonication (Fisherbrand™ FB-505) to ensure proper dispersion. The CNT/CMC solution was then spray-coated onto the plasma-treated substrates using a programmable spray system (Krautzberger GmbH, Germany) to achieve controlled film thickness [46, 47]. The deposited films were rinsed thoroughly with deionized water to remove residual nitric acid, used earlier in the CNT functionalization process, and any excess binder. After rinsing, the films were dried at 100 °C on a hotplate to ensure complete solvent removal. Silver (Ag) conductive tracks were patterned on top of the CNT layer via screen printing (Aurel automation S.P.A, C290), using a mesh mask to define the electrode geometry, as illustrated in Figure 1b (electrode dimensions) and Figure 1c (device cross-section). The designed sensor features interdigitated electrodes with a line width and spacing of 300 µm, and an active sensing area of 29 mm^2. This geometry increases the effective sensing path between adjacent fingers, enhancing resistance modulation during gas exposure [29], while maintaining printing resolution and minimizing variability [30]. Finally, the entire device was thermally cured in the oven (Falc Instruments s.r.l) at 120 °C for 20 min to improve mechanical stability and ensure robust electrical contact between the CNT network and the Ag electrodes.

4.2 | Electrical Measurements in Dry Air and UHV

Prior to electrical measurements in both dry air and UHV, the samples were preheated at 60 °C for 30–60 min to remove adsorbed moisture and stabilize the baseline resistance. We then performed electrical characterization of the chemoresistive sensor's response to NH_3 in dry air using a custom-built gas chamber. The chamber is equipped with a Peltier element for temperature control and integrated temperature and humidity sensors. Resistance measurements were recorded using a Keithley DAQ6510 digital multimeter, while two Keithley 2602B source meters powered the Peltier element. NH_3 test atmospheres were generated using a mass flow controller (Bronkhorst) to regulate gas mixing, with dry compressed air acting as the carrier gas. The total flow rate was kept constant at 450 mL/min, and NH_3 concentrations of 3, 10, 25, and 50 ppm were obtained by diluting gas from an NH_3 and dry air cylinders. Each sensing cycle consisted of a 10-min baseline stabilization period in dry air, a 5-min exposure period at the target NH_3 concentration, and an active recovery period of 15 min at 60 °C via Peltier heating to accelerate desorption. Electrical measurements were also performed under UHV available conditions in the XPS chamber at the ESCAmicroscopy beamline using a Keithley 2612B source-measure unit. A constant bias was applied across the CNT chemoresistor by electrically connecting the screen-printed Ag electrodes through the sample holder. The resulting current was recorded throughout the SPEM experiments.

4.3 | Spatially Resolved SPEM-XPS of CNT Sensors Under Dynamic High-Pressure NH_3 Dosing

XPS measurements were conducted at the ESCAmicroscopy beamline of the Elettra synchrotron (Trieste, Italy) [26, 27, 35]. These in situ XPS experiments were carried out to investigate the surface chemistry of our CNT-based sensors within the interdigitated spacing region before, during, and after NH_3 exposure. A photon energy of 649.3 eV was used to collect high-resolution C 1s spectra. Samples, mounted on a conductive holder, were introduced into a UHV chamber (base pressure $\sim 1 \times 10^{-9}$ mbar). Scanning photoelectron microscopy (SPEM) was employed to obtain spatially resolved C 1s intensity maps with a spatial resolution of 10 µm, corresponding to the focused beam size during surface scanning. XPS spectra were recorded with the beam focused to a 75 µm spot size, positioned within the spacing region between the interdigitated electrodes. Spectra were collected using a hemispherical analyzer, providing an overall energy resolution of 180 meV. NH_3 (≥99.5 % purity) was supplied from a 3.5 bar gas cylinder through a 0.5 mm stainless-steel needle positioned a few millimeters above the sample. Controlled pulses (2.42 ms each) were delivered at 0.3 Hz via a precision leak valve, maintaining the chamber pressure at $\sim 1 \times 10^{-6}$ mbar during dosing. C 1s spectra were acquired before, during, and after NH_3 dosing.

Acknowledgements

This research was funded by the Italian Ministry of University and Research (MUR) through the PRIN 2022 Projects 2D-EMMA (Project n. 202289PMBP, CUP: B53D23004010006) and PETRA (Project n. 2022T7ZSEK, CUP: B53D23001860006). It also received funding from Next Generation EU through the PNRR 2023 Project NQSTI (Project n. PE0000023, CUP: B53C22004180005) and from the European Union Next-GenerationEU (PIANO NAZIONALE DI RIPRESA E RESILIENZA (PNRR)—MISSIONE 4 COMPONENTE 2, INVESTIMENTO 1.4—D.D. 1032 17/06/2022, CN00000022).

Conflicts of Interest

The authors declare no conflicts of interest.

Data Availability Statement

The data that support the findings of this study are available from the corresponding authors upon reasonable request.

References

1. R. Tang, Y. Shi, Z. Hou, and L. Wei, "Carbon Nanotube-Based Chemiresistive," *Sensors* 17 (2017): 882, https://doi.org/10.3390/s17040882.

2. S.-Y. Guo, P.-X. Hou, F. Zhang, C. Liu, and H.-M. Cheng, "Gas Sensors Based on Single-Wall Carbon Nanotubes," *Molecules* 27 (2022): 5381, https://doi.org/10.3390/molecules27175381.

3. C. Wang, L. Yin, L. Zhang, D. Xiang, and R. Gao, "Metal Oxide Gas Sensors: Sensitivity and Influencing Factors," *Sensors* 10 (2010): 2088–2106, https://doi.org/10.3390/s100302088.

4. R. R. Kumar, M. R. Habib, A. Khan, et al., "Sulfur Monovacancies in Liquid-Exfoliated MoS_2 Nanosheets for NO_2 Gas Sensing," *ACS Applied Nano Materials* 4 (2021): 9459–9470, https://doi.org/10.1021/acsanm.1c01929.

5. R. R. Kumar, S. Gupta, A. K. Anbalagan, et al., "Time-Dependent Growth of Sputtered MoS_2 Films on ZnO Nanorods for Enhanced NO_2 Sensing Performance," *Micromachines* 16 (2025): 659, https://doi.org/10.3390/mi16060659.

6. R. R. Kumar, S. Gupta, H.-F. Huang, T. Murugesan, N.-H. Tai, and H.-N. Lin, "Light Intensity Effects on the Performance of In_2O_3 Gas Sensors: Insights into Adsorption and Desorption Dynamics," *Materials Chemistry and Physics* 337 (2025): 130639, https://doi.org/10.1016/j.matchemphys.2025.130639.

7. X. Huang, R. Pang, M. Yang, et al., "Flexible Gas Sensors Based on Carbon Nanotube Hybrid Films: A Review," *Advanced Materials Technologies* 8 (2023): 2300616, https://doi.org/10.1002/admt.202300616.

8. K. Luo, H. Peng, B. Zhang, et al., "Advances in Carbon Nanotube-Based Gas Sensors: Exploring the Path to the Future," *Coordination Chemical Reviews* 518 (2024): 216049, https://doi.org/10.1016/j.ccr.2024.216049.

9. V. Pecunia, L. Petti, J. B. Andrews, et al., "Roadmap on Printable Electronic Materials for Next-Generation Sensors," *Nano Futures* 8 (2024): 032001, https://doi.org/10.1088/2399-1984/ad36ff.

10. S.-X. L. Luo and T. M. Swager, "Chemiresistive Sensing with Functionalized Carbon Nanotubes," *Nature Reviews Methods Primers* 3 (2023): 73, https://doi.org/10.1038/s43586-023-00255-6.

11. S. D. Lawaniya, S. Kumar, Y. Yu, and K. Awasthi, "Nitrogen-Doped Carbon Nano-Onions/Polypyrrole Nanocomposite Based Low-Cost Flexible Sensor for Room Temperature Ammonia Detection," *Scientific Reports* 14 (2024): 7904, https://doi.org/10.1038/s41598-024-57153-4.

12. A. Boyd, I. Dube, G. Fedorov, M. Paranjape, and P. Barbara, "Gas Sensing Mechanism of Carbon Nanotubes: From Single Tubes to High-Density Networks," *Carbon* 69 (2014): 417–423, https://doi.org/10.1016/j.carbon.2013.12.044.

13. C. Wei, L. Dai, A. Roy, and T. B. Tolle, "Multifunctional Chemical Vapor Sensors of Aligned Carbon Nanotube and Polymer Composites," *Journal of American Chemical Society* 128 (2006): 1412–1413, https://doi.org/10.1021/ja0570335.

14. L. Zeininger, M. He, S. T. Hobson, and T. M. Swager, "Resistive and Capacitive γ-Ray Dosimeters Based On Triggered Depolymerization in Carbon Nanotube Composites," *ACS Sensors* 3 (2018): 976–983, https://doi.org/10.1021/acssensors.8b00108.

15. K. Tanaka, G. Cheng, T. Nakamura, et al., "NH_3 Gas Sensors Based on Single-Walled Carbon Nanotubes Interlocked with Metal-Tethered Tetragonal Nanobrackets," *ACS Applied Nano Materials* 7 (2024): 13417–13425, https://doi.org/10.1021/acsanm.4c01880.

16. K. Kawasaki, I. Harada, K. Akaike, et al., "Complex Chemistry of Carbon Nanotubes Toward Efficient and Stable P-Type Doping," *Communications Materials* 5 (2024): 21, https://doi.org/10.1038/s43246-024-00460-0.

17. V. Schroeder, S. Savagatrup, M. He, S. Lin, and T. M. Swager, "Carbon Nanotube Chemical Sensors," *Chemical Reviews* 119 (2019): 599–663, https://doi.org/10.1021/acs.chemrev.8b00340.

18. R. Zhang, M. Zhu, T. Tian, et al., "Fermi Level Regulation of Single-Walled Carbon Nanotubes by Metal Chloride Doping for Enhanced NO2 Sensing Performance," *Diamond and Related Materials* 151 (2025): 111777, https://doi.org/10.1016/j.diamond.2024.111777.

19. A. Salehi-Khojin, F. Khalili-Araghi, M. A. Kuroda, K. Y. Lin, J.-P. Leburton, and R. I. Masel, "On the Sensing Mechanism in Carbon Nanotube Chemiresistors," *ACS Nano* 5 (2011): 153–158, https://doi.org/10.1021/nn101995f.

20. I. J. T. Jensen, A. Ali, P. Zeller, et al., "Direct Observation of Charge Transfer between NO_x and Monolayer MoS_2 by Operando Scanning Photoelectron Microscopy," *ACS Applied Nano Materials* 4 (2021): 3319–3324, https://doi.org/10.1021/acsanm.1c00137.

21. L. S. Panchakarla, A. Govindaraj, and C. N. R. Rao, "Nitrogen- and Boron-Doped Double-Walled Carbon Nanotubes," *ACS Nano* 1 (2007): 494–500, https://doi.org/10.1021/nn700230n.

22. A. M. Rao, P. C. Eklund, S. Bandow, A. Thess, and R. E. Smalley, "Evidence for Charge Transfer in Doped Carbon Nanotube Bundles From Raman Scattering," *Nature* 388 (1997): 257–259, https://doi.org/10.1038/40827.

23. R. Voggu, C. S. Rout, A. D. Franklin, T. S. Fisher, and C. N. R. Rao, "Extraordinary Sensitivity of the Electronic Structure and Properties of Single-Walled Carbon Nanotubes to Molecular Charge-Transfer," *The Journal of Physical Chemistry C* 112 (2008): 13053–13056, https://doi.org/10.1021/jp805136e.

24. A. Gurlo and R. Riedel, "Situ and Operando Spectroscopy for Assessing Mechanisms of Gas Sensing," *Angewandte Chemie International Edition* 46 (2007): 3826–3848, https://doi.org/10.1002/anie.200602597.

25. A.-K. Elger and C. Hess, "Application of Raman Spectroscopy to Working Gas Sensors: From In Situ to Operando Studies," *Sensors* 19 (2019): 5075, https://doi.org/10.3390/s19235075.

26. M. Amati, L. Gregoratti, P. Zeller, et al., "Near Ambient Pressure Photoelectron Spectro-Microscopy: From Gas–Solid Interface to Operando Devices," *Journal of Physics D Applied Physics* 54 (2021): 204004, https://doi.org/10.1088/1361-6463/abe5e2.

27. M. Amati, L. Yashina, P. Winkler, et al., "Catalytically Active Materials Visualized by Scanning Photoelectron Spectro-Microscopy," *Surfaces* 7 (2024): 442–459, https://doi.org/10.3390/surfaces7030028.

28. B. B. Shirvani, J. Beheshtian, G. Parsafar, and N. L. Hadipour, "DFT study of $NH_3(H_2O)_{n=0,1,2,3}$ Complex Adsorption on the (8,0) Single-Walled Carbon Nanotube," *Computational Materials Science* 48 (2010): 655–657, https://doi.org/10.1016/j.commatsci.2010.02.035.

29. S. Vasquez, M. A. C. Angeli, A. Polo, et al., "In Vitro Gastrointestinal Gas Monitoring with Carbon Nanotube Sensors," *Scientific Reports* 14 (2024): 825, https://doi.org/10.1038/s41598-023-50134-z.

30. S. Vasquez, M. A. Costa Angeli, M. Petrelli, et al., "Comparison of Printing Techniques for the Fabrication of Flexible Carbon Nanotube-Based Ammonia Chemiresistive Gas Sensors," *Flexible and Printed Electronics* 8 (2023): 035012, https://doi.org/10.1088/2058-8585/acef39.

31. L. Valentini, C. Cantalini, I. Armentano, J. M. Kenny, L. Lozzi, and S. Santucci, "Highly Sensitive and Selective Sensors Based on Carbon Nanotubes Thin Films for Molecular Detection," *Diamond and Related Materials* 13 (2004): 1301–1305, https://doi.org/10.1016/j.diamond.2003.11.011.

32. F. Rigoni, S. Tognolini, P. Borghetti, et al., "Enhancing the Sensitivity of Chemiresistor Gas Sensors Based on Pristine Carbon Nanotubes to Detect Low-Ppb Ammonia Concentrations in the Environment," *Analyst* 138 (2013): 7392–7399, https://doi.org/10.1039/c3an01209c.

33. O. K. Varghese, P. D. Kichambre, D. Gong, K. G. Ong, E. C. Dickey, and C. A. Grimes, "Gas Sensing Characteristics of Multi-Wall Carbon Nanotubes," *Sensors and Actuators, B: Chemical* 81 (2001): 32–41, https://doi.org/10.1016/S0925-4005(01)00923-6.

34. M. N. Norizan, N. D. Siti Zulaikha, A. B. Norhana, M. I. Syakir, and A. Norli, "Carbon Nanotubes-Based Sensor for Ammonia Gas Detection – An Overview," *Polimery* 66 (2021): 175–186, https://doi.org/10.14314/polimery.2021.3.3.

35. M. Amati, M. K. Abyaneh, and L. Gregoratti, "Dynamic High Pressure: A novel Approach Toward Near Ambient Pressure Photoemission Spectroscopy and Spectromicroscopy," *Journal of Instrumentation* 8 (2013), https://doi.org/10.1088/1748-0221/8/05/T05001.

36. D. Kang, N. Park, J. Ko, E. Bae, and W. Park, "Oxygen-Induced P-Type Doping of a Long Individual Single-Walled Carbon Nanotube," *Nanotechnology* 16 (2005): 1048–1052, https://doi.org/10.1088/0957-4484/16/8/008.

37. J. Kong, N. R. Franklin, C. Zhou, et al., "Nanotube Molecular Wires as Chemical Sensors," *science* 287 (2000): 622–625, https://doi.org/10.1126/science.287.5453.622.

38. T. A. Saleh, "Isotherm Models of Adsorption Processes on Adsorbents and Nanoadsorbents," *Interface Science and Technology* 34 (2022): 99–126, https://doi.org/10.1016/B978-0-12-849876-7.00009-9.

39. C. Wen, Q. Ye, S.-L. Zhang, and D. Wu, "Assessing kinetics of Surface Adsorption–Desorption of Gas Molecules via Electrical Measurements," *Sensors and Actuators, B: Chemical* 223 (2016): 791–798, https://doi.org/10.1016/j.snb.2015.10.019.

40. K. A. Babatunde, B. M. Negash, S. R. Jufar, T. Y. Ahmed, and M. R. Mojid, "Adsorption of Gases on Heterogeneous Shale Surfaces: A Review," *Journals of Petroleum Science and Engineering* 208 (2022): 109466, https://doi.org/10.1016/j.petrol.2021.109466.

41. S. Kasap, *Principles of Electronic Materials and Devices*, (McGraw-Hill, Inc., 2006).

42. N. Barsan and U. Weimar, "Conduction Model of Metal Oxide Gas Sensors," *Journals of Electroceramics* 7 (2001): 143–167, https://doi.org/10.1023/A:1014405811371.

43. D. Degler, U. Weimar, and N. Barsan, "Current Understanding of the Fundamental Mechanisms of Doped and Loaded Semiconducting Metal-Oxide-Based Gas Sensing Materials," *ACS Sensors* 4 (2019): 2228–2249, https://doi.org/10.1021/acssensors.9b00975.

44. N. Kaur, M. Singh, and E. Comini, "One-Dimensional Nanostructured Oxide Chemoresistive Sensor," *Langmuir* 36 (2020): 6326–6344, https://doi.org/10.1021/acs.langmuir.0c00701.

45. B. Shkodra, B. Demelash Abera, G. Cantarella, et al., "Flexible and Printed Electrochemical Immunosensor Coated with Oxygen Plasma Treated SWCNTs for Histamine Detection," *Biosensors* 10 (2020): 35, https://doi.org/10.3390/bios10040035.

46. M. Petrelli, B. Shkodra, A. Falco, et al., "From Rigid to Flexible: Solution-Processed Carbon Nanotube Deposition on Polymeric Substrates for the Fabrication of Transistor-Based Ion Sensors," *IEEE Journal on Flexible Electronics* 2 (2023): 300–307, https://doi.org/10.1109/JFLEX.2023.3303149.

47. P. Lugli, M. Petrelli, B. Shkodra, et al., "Solution-Processable Carbon Nanotubes for Sensing and Biosensing Applications," in 2023 IEEE Nanotechnology MaterIals and Devices Conference NMDC, (IEEE, 2023): pp. 655–659, https://doi.org/10.1109/NMDC57951.2023.10343652.

Supporting Information

Additional supporting information can be found online in the Supporting Information section.

Supporting File 1: admi70355-sup-0001-SuppMat.docx